Progress In Electromagnetics Research C, Vol. 171, 482–491, 2026 PIER C

(Received 6 May 2026, Accepted 15 June 2026, Scheduled 16 July 2026)

Wideband 8-Antenna Array Design for Low Profile Metal Frame 5G Smartphones

Rong Cao*, Chun-Yi Chen, and Wei-Chih Wang

Department of Electrical Engineering, Feng Chia University, Taichung 40724, Taiwan, R.O.C.

ABSTRACT: This paper presents a compact wideband eight-antenna array for sub-7 GHz 5G smartphone applications with a low-profile metal frame. By employing a multi-near-circular open-slot configuration integrated into the system ground and metal frame, the proposed design achieves wideband operation from 3.3 to 7.125 GHz, covering 5G NR bands n77/n78/n79 and NR-U bands n46/n96, without requiring additional decoupling structures. The antenna element occupies a compact volume of $8 \times 3.5 \times 4\,\text{mm}^3$, enabling a low-profile implementation compatible with modern smartphone form factors. Measured results demonstrate a 6-dB impedance bandwidth, fully covering the target bands, with inter-element isolation higher than 10 dB and an envelope correlation coefficient (ECC) below 0.1. The measured total efficiency ranges from 40% to 77% across the operating band. Furthermore, the antenna array maintains stable performance under practical conditions, including hand and battery effects. The proposed design offers a simple and effective solution for achieving wideband, low-profile, and low-correlation MIMO performance in metal-frame smartphones.

1. INTRODUCTION

The development of fifth-generation (5G) mobile communication systems has been rapidly advancing in recent years. Driven by the increasing demand for high data throughput and improved spectrum efficiency in emerging applications, such as artificial intelligence (AI), the Internet of Things (IoT), and smart cities, wideband operation has become a critical requirement for modern 5G systems. The Fifth Generation New Radio (5G NR) standard specifies several sub-6 GHz frequency bands, including n77 (3.3–4.2 GHz), n78 (3.3–3.8 GHz), and n79 (4.4–5.0 GHz). To meet the high data-rate requirements in these bands, multi-input multi-output (MIMO) technology has been widely adopted, as it significantly enhances the spectrum efficiency and channel capacity [1–3]. In addition to the licensed spectrum, the utilization of unlicensed frequency bands has attracted increasing attention in recent years. In particular, the Unlicensed National Information Infrastructure (U-NII) bands have been incorporated into 5G New Radio Unlicensed (NR-U), including bands n46 (5.15–5.925 GHz) and n96 (5.925–7.125 GHz) [4]. This trend further expands the required operating bandwidth of smartphone antennas, making wideband antenna design more challenging.

Early 5G smartphone antenna designs typically adopted quarter-wavelength ($\lambda/4$) open-slot or monopole structures to excite a fundamental resonance at approximately 3.5 GHz [5, 6]. However, as antennas are increasingly integrated into the metal frame of smartphones, inverted-F antennas (IFAs) and loop antennas have become more prevalent due to their structural compatibility and compact size [7, 8]. To further enhance the operating bandwidth, hybrid configurations combining these antenna types have been proposed in recent studies [9–11].

When multiple antennas are embedded within the constrained space of a smartphone, mutual electromagnetic coupling inevitably degrades antenna isolation. To address this challenge, various isolation enhancement methodologies have been extensively investigated in the literature. For instance, the deployment of dedicated decoupling structures [12–14] can effectively suppress the coupling energy between adjacent elements. Alternatively, polarization orthogonalization [15–17] leverages polarization diversity to inherently enhance isolation. Moreover, self-isolated designs [18–22] mitigate the impact of shared ground-plane currents, thereby improving isolation efficiency. To better align with modern market demands, diverse metal-frame multi-antenna array designs [9–17, 21, 22] have also been widely reported. However, these approaches often increase structural complexity, require additional design space, or impose constraints on antenna configuration.

Meanwhile, recent studies have focused on extending the operating bandwidth toward the sub-7 GHz range to support both licensed and unlicensed 5G bands [23–26]. Although wideband performance has been achieved in these studies, realizing an ultra-low-profile design with a height below 5 mm while simultaneously maintaining wide bandwidth and satisfactory isolation remains challenging.

To address these challenges, this study proposes a wideband eight-antenna array for sub-7 GHz 5G smartphone applications with a low-profile metal frame. By employing a multi-near-circular open-slot configuration integrated into both the system ground and the metal frame, multiple resonant modes are excited and effectively merged to achieve continuous wideband operation from 3.3 to 7.125 GHz. Furthermore, by properly

* Corresponding author: Rong Cao (rcao@fcu.edu.tw).

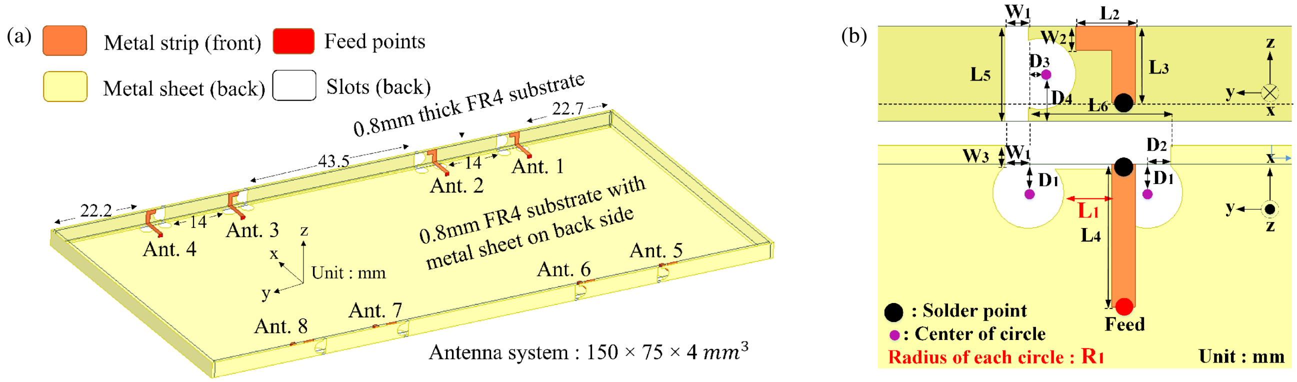

FIGURE 1. The design of the proposed antenna: (a) design of the eight-element antenna array and (b) structure of a single antenna element ($R_1 = 1.5$, $L_1 = 2$, $L_2 = 2.5$, $L_3 = 3.2$, $L_4 = 6$, $L_5 = 4$, $L_6 = 6$, $W_1 = 1$, $W_2 = 1$, $W_3 = 0.88$, $D_1 = 1$, $D_2 = 1$, $D_3 = 0.5$, $D_4 = 2$, unit: mm).

optimizing the element placement and the geometry of near-circular open slots, the proposed configuration achieves sufficient isolation between adjacent elements, thereby eliminating the need for additional decoupling structures.

The main contributions of this study can be summarized as follows. First, a compact antenna element with a height of only 4 mm is developed, achieving wideband coverage across 3.3–7.125 GHz, including both 5G NR and NR-U bands. Second, a multi-input multi-output (MIMO) configuration is realized within a constrained space, achieving an Envelope Correlation Coefficient (ECC) below 0.1 across the entire operating band without employing any extra decoupling structures. Third, the proposed design is validated through comprehensive simulations and measurements, including S-parameters, radiation patterns, efficiency, ECC, channel capacity, and Total Active Reflection Coefficient (TARC). Finally, the robustness of the antenna array is verified under practical conditions, including hand and battery effects.

The remainder of this paper is organized as follows. Section 2 describes the antenna configuration and geometry. Section 3 presents the design evolution and operating mechanism. Section 4 discusses parametric analysis. Section 5 provides the measured results and discussions, followed by the conclusion in Section 6.

2. ANTENNA DESIGN AND GEOMETRY

Figure 1(a) shows the design of an eight-antenna array integrated into a low-profile metal-framed smartphone. The structure consists of a system circuit board of size 150 mm × 75 mm (with a ground plane on the back side) and a 4-mm-high metal frame surrounding the ground plane on all four sides. Both the ground plane and the metal frame were implemented on a 0.8 mm FR4 substrate ($\varepsilon_r = 4.4$, loss tangent $= 0.02$). The proposed eight-antenna array (Ant. 1–Ant. 8) is divided into two four-antenna sub-arrays (Ant. 1–Ant. 4 and Ant. 5–Ant. 8), which are arranged along the left and right long edges of the metal frame, respectively. The two sub-arrays are symmetric with respect to each other and the center of the ground plane. For simplicity, only Ant. 1–Ant. 4 are discussed herein.

Owing to the allocation of two clearance regions of size 75 mm × 22 mm at the top and bottom of the smartphone for other antennas (e.g., 3G/4G/WLAN/WiFi), Ant. 1 and Ant. 4 are positioned 22.7 and 22.2 mm from the top-left and bottom-left corners, respectively. To achieve good impedance matching and satisfactory isolation between adjacent elements, the feeding structures of Ant. 1–Ant. 2 and the orientations of the near-circular slots were designed to be opposite to those of Ant. 3–Ant. 4. The spacing between Ant. 2 and Ant. 3 was 43.5 mm, whereas that between Ant. 1 and Ant. 2 (and Ant. 3 and Ant. 4) is 14 mm.

Figure 1(b) illustrates the detailed geometry of the proposed antenna element (Ant. 1). A 50-Ω inverted L-shaped microstrip feeding strip was used to excite both the ground and vertical slots located on the outer side of the metal frame. The ground slot consists of a $7 \times 1\ \text{mm}^2$ horizontal slot and two near-circular slots with a radius of 1.5 mm, while the vertical slot on the metal frame comprises a straight slot and a near-circular slot. Crucially, these near-circular slots are designed to overlap and merge with their adjacent straight/horizontal slots. Their relative positions are defined by the center-to-edge distances, D_1 and D_3.

3. DESIGN PROCESS AND METHODOLOGY

3.1. Evolution of the Antenna

Figure 2(a) is the flowchart of the antenna element design process, and Fig. 2(b) shows the simulated return losses of Ref. 1, Ref. 2, Ref. 3, Ref. 4, and the proposed antenna. It should be noted that the performance of the antenna element is characterized within the complete smartphone environment by terminating the other elements with 50-Ohm loads. Following the practical design considerations for 5G mobile terminals, a −6 dB reflection-coefficient criterion is implemented herein to evaluate the impedance bandwidth and parametric performance. This criterion is widely adopted in modern smartphone antenna design due to the severe space constraints, which differ from stationary systems.

The initial design (Ref. 1) is a 50 Ω straight strip feeding an L-shaped slot (a combination of a horizontal and a vertical slot), which serves as the embryonic stage in the antenna evo-

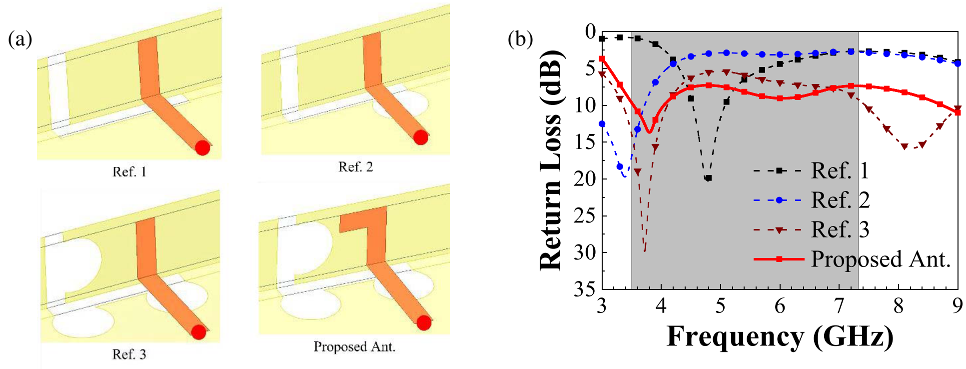

FIGURE 2. (a) Evolution of the antenna design and (b) simulated return loss of Ref. 1, Ref. 2, Ref. 3 and the proposed antenna.

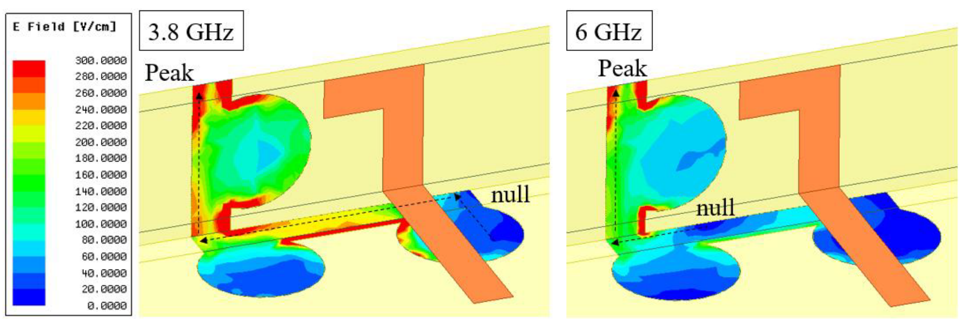

FIGURE 3. The electric-field distribution of the proposed antenna at 3.8 GHz and 6 GHz.

lution. This initial configuration excites a fundamental quarter-wavelength resonance f_1 at 4.8 GHz. While Ref. 1 provides a baseline resonance, subsequent structural modifications are necessary. To excite a new resonant mode, the antenna in Ref. 2 was proposed by introducing a near-circular slot on the right side of the ground slot from Ref. 1. This modification shifts the first resonant frequency (f_1) to 3.4 GHz and induces a weak initial resonant trend around 6 GHz (f_2). However, the impedance matching in the 6 GHz band remains poor.

To improve impedance matching and extend the band, Ref. 3 introduces a pair of near-circular slots (one extending from the vertical frame slot toward the feeding strip, and the other extending from the left edge of the ground slot). This modification alters local boundary conditions and lengthens the electrical path around the aperture, shifting the f_1 resonance upward to optimize mode spacing while exciting a new higher-order resonance f_3 beyond 8 GHz. Rather than aiming for a sharp independent resonance, this multi-slot configuration provides extra tuning freedom that flattens the reflection coefficient profile, extending the bandwidth potential up to 7.125 GHz. However, matching around 5 GHz remains insufficient for a fully continuous wideband response. To address this, the proposed antenna utilizes an inverted L-shaped feeding strip, shifting the f_2 resonant behavior down by 0.6 GHz to improve bandwidth matching. The final impedance bandwidth is cooperatively shaped by the primary f_1 resonance (3.8 GHz), a secondary resonance-assisted behavior near 6 GHz (f_2) contributing to wideband formation, and a resonant response (f_3) beyond 9 GHz. These behaviors merge to deliver a continuous wideband profile, allowing the antenna to fully cover the 5G NR n77/n78/n79 and 5G NR-U n46/n96 frequency bands.

3.2. E-Field Distribution of the Antenna

To investigate the operating mechanism and excitation behavior of the proposed antenna within the terminal environment, the simulated E-field distributions at the primary resonant frequencies are analyzed, as shown in Fig. 3. This localized physical insight allows for a direct evaluation of how the slot configuration interacts with the adjacent structure. As illustrated in the full-wave simulation results, the proposed slot element effectively couples electromagnetic energy into the metal frame and chassis, guiding the structural currents to achieve optimal radiation and decoupling performance.

Specifically, at 3.8 GHz, the antenna excites a fundamental quarter-wavelength resonant mode. The physical radiating path is approximately 12.4 mm, which correlates closely with the theoretical quarter-wavelength of 11.8 mm. At 6 GHz, a second quarter-wavelength resonant mode is generated, with its electric-field null strategically positioned between the two near-circular ground slots. By effectively merging these two resonant modes, the proposed antenna achieves continuous wideband coverage across the 5G NR n77/n78/n79 and 5G NR-U n46/n96 bands.

3.3. MIMO Pattern Diversity Logic and Correlation Analysis

The operating principle of the proposed array is based on the spatial placement and slot-induced perturbation of the antenna

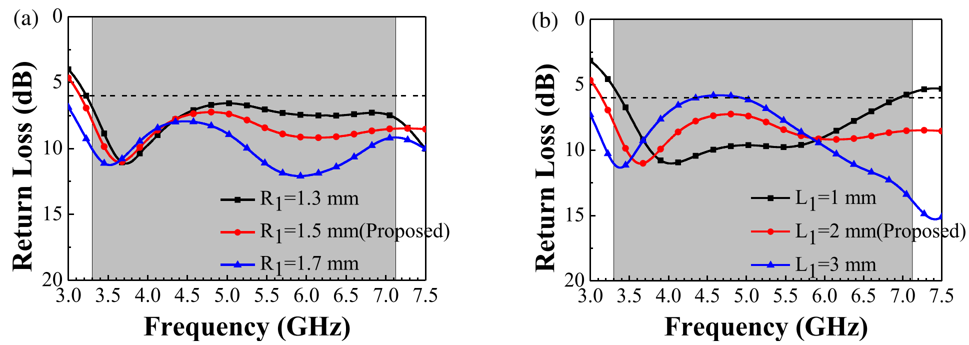

FIGURE 4. Parametric analysis of S_{11} performance with variations in (a) R_1 and (b) L_1.

elements integrated into the metal frame. The primary mechanism for achieving robust MIMO performance relies on promoting pattern diversity and reducing radiation correlation between adjacent elements, rather than solely relying on high near-field isolation. By optimizing the placement and geometry of the near-circular slots, a controlled boundary perturbation is introduced into the aperture field distribution. This perturbation alters the characteristic radiation patterns of adjacent antennas and promotes greater pattern diversity. As a result, the measured ECC remains below 0.1 across the wide 3.3–7.125 GHz operating band despite the moderate isolation level between adjacent elements. This pattern-diversity-oriented design approach enables the proposed eight-antenna system to maintain stable MIMO performance and channel capacities of 35.7–41.4 bps/Hz within a compact metal-frame smartphone platform, providing a practical solution for wideband multi-antenna integration without requiring complex decoupling structures.

4. PARAMETER ANALYSIS

The systematic investigation of the key geometric parameters R_1 and L_1 (indicated in red in Fig. 1(b)) was conducted to explore the tunability and optimize the impedance matching within the 4-mm low-profile constraint. To properly evaluate individual element's characteristics under a smartphone environment, the simulated results are obtained by exciting one specific port while terminating the remaining ports with 50-Ohm loads. It should be noted that although this parametric optimization focuses on a single antenna element, the geometrical variations are synchronously applied to all elements across the entire array layout to preserve structural uniformity and symmetry.

R_1 represents the radius of the near-circular ground slots, and its effect is illustrated in Fig. 4(a). Due to structural constraints, the center-to-edge distances (from the circular slot centers to the adjacent vertical and horizontal strip slot boundaries) are fixed at 0.5 mm (D_3) and 1 mm (D_1), respectively. To focus on the intended overlapping slot configurations, simulations for $R_1 < 1$ mm were omitted. The results indicate that increasing R_1 significantly enhances the impedance matching of the f_2 resonant mode at 6 GHz. However, to ensure sufficient mechanical robustness of the ultra-thin metal frame, the final value of R_1 was optimized to 1.5 mm, balancing the electromagnetic performance with the structural integrity.

L_1 is the lateral distance between the feeding strip and the left near-circular slot. As shown in Fig. 4(b), increasing L_1 shifts the fundamental mode f_1 (3.8 GHz) toward lower frequencies while slightly pushing the f_2 mode (6.0 GHz) higher. Consequently, reducing L_1 effectively narrows the frequency ratio between f_1 and f_2, facilitating the merging of these two resonances to achieve a contiguous wideband response. This behavior aligns with the E-field distributions in Fig. 3, where an increase in L_1 lengthens the effective current path for the 3.8 GHz resonance but has a negligible impact on the 6.0 GHz mode. Although $L_1 = 1$ mm provides good matching between the two peaks, it fails to provide the necessary bandwidth margin for the higher 5G NR-U bands. Therefore, $L_1 = 2$ mm was selected to ensure full and stable coverage across the n77/n78/n79 and n46/n96 frequency bands.

5. RESULTS AND DISCUSSION

5.1. S-Parameters

A proposed low-profile metal-framed wideband eight-antenna array was fabricated. Photographs of this antenna are shown in Fig. 5. To validate the simulated results, a prototype of the proposed antenna was fabricated and characterized. The S-parameters were measured using a Rohde & Schwarz Vector Network Analyzer (VNA) after performing a standard Short-Open-Load-Thru (SOLT) calibration to eliminate cable and adapter errors. All far-field antenna parameters reported herein were validated using the Satimo StarLab system, which employs the spherical near-field measurement technique. During both the S-parameter and radiation pattern measurements, all unused antenna ports were terminated with standard 50 Ω dummy loads to prevent unwanted reflections or mutual coupling.

Figure 6 illustrates the superimposed simulated and measured reflection coefficients of the representative elements (Ant. 1 and Ant. 2) for direct comparison. Due to the near-symmetry of the proposed 8-antenna array, curves for the remaining elements are omitted to maintain visual clarity. As observed in Fig. 6, noticeable discrepancies between the simulated and measured results are present throughout the frequency range, particularly in the form of resonant frequency shifts and fluctuations in reflection depths. These deviations may be mainly attributed to the idealized lumped-port excitation

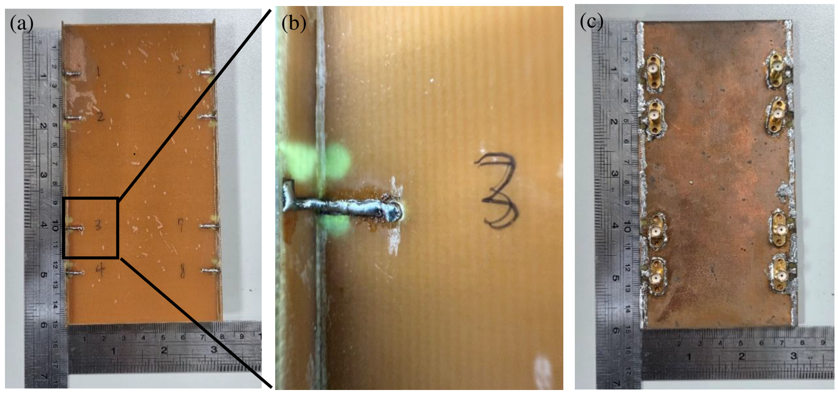

FIGURE 5. Photograph of the fabricated antenna array: (a) front view, (b) close-up view of Ant. 3, and (c) back view.

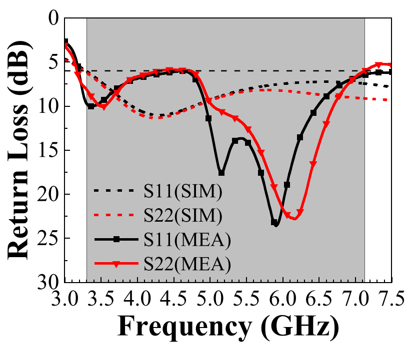

FIGURE 6. Simulated and measured return losses of the proposed array antenna (Ant. 1 and Ant. 2).

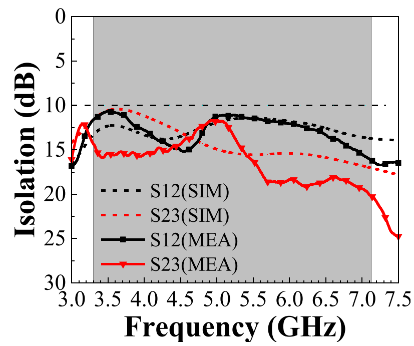

FIGURE 7. Simulated and measured isolation between antenna elements (Ant. 1–Ant. 2 and Ant. 2–Ant. 3).

employed in the simulations, which omits the intricate physical geometry of the SMA connectors and soldered feeding lines. Consequently, the fabricated prototype experiences additional port parasitic effects, slot-etching variations, and soldering non-idealities that perturb input impedance. Nevertheless, the measured impedance response remains below the -6 dB reference line across the entire target spectrum, confirming continuous wideband operation.

Figure 7 presents superimposed simulated and measured isolation characteristics of the representative antenna pairs. Due to array symmetry, only key curves are depicted for visual clarity. As observed, although some discrepancies exist, the measured isolation generally follows a compatible trend with the simulations. Consistent with the reflection-coefficient analysis, these deviations may be mainly attributed to the idealized lumped-port excitation used in simulations, which omits the practical geometry of SMA connectors and manually assembled feeding lines. Consequently, the fabricated prototype is more susceptible to slot-etching variations, manual soldering non-idealities, and assembly alignment errors. Nevertheless, the measured isolation consistently remains below the 10 dB threshold across the target 3.3–7.125 GHz band, confirming that the decoupling performance is robust and fully acceptable for mobile terminals.

5.2. Radiation Performances

Figure 8 shows simulated and measured total efficiencies of the proposed antenna array, fluctuating between 48.3% and 73.6%

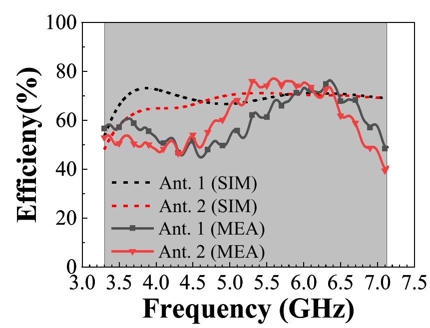

FIGURE 8. Simulated and measured efficiencies of the proposed array antenna (Ant. 1 and Ant. 2).

and between 39.5% and 77.3%, respectively. As anticipated, these numerical discrepancies may be mainly attributed to the idealized excitation model and simplified material parameters used in simulations. In the lower range, the omitted SMA geometry, soldering non-idealities, and frequency-dependent substrate losses inevitably introduce additional energy dissipation, degrading the measured efficiency. Conversely, around 6 GHz, the measured efficiency outperforms the simulated one. This variation is primarily because the port parasitic effects and fabrication variations accidentally introduce a slightly better impedance matching condition in this specific band, as evidenced by the deeper measured resonance in Fig. 6.

In addition, the measured peak gain of the antenna elements varies from -0.35 to 5.36 dBi across the target frequency band

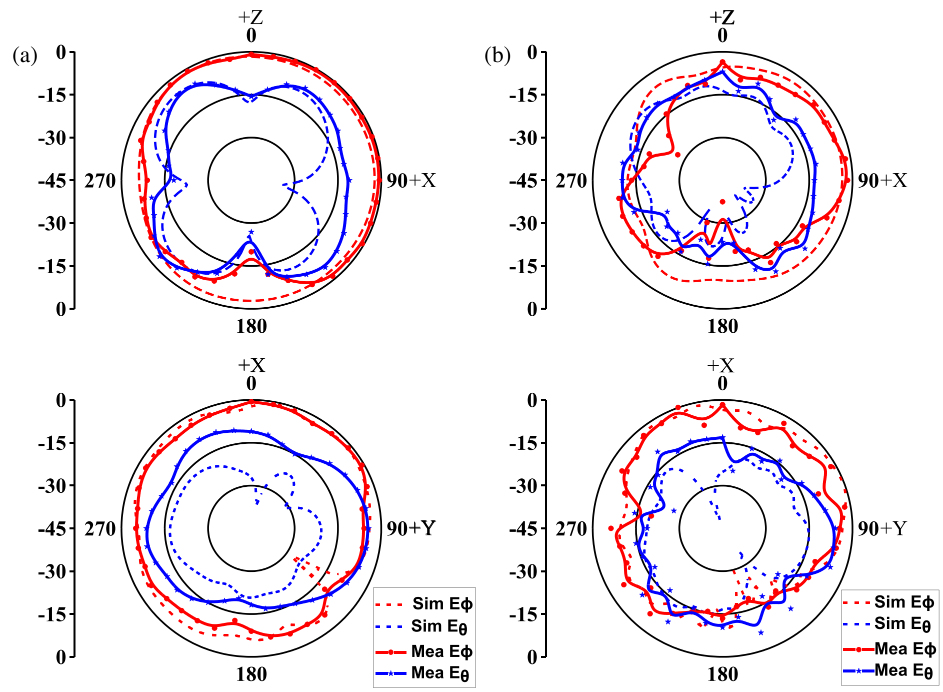

FIGURE 9. Normalized radiation patterns of Ant. 1 at: (a) 3.5 GHz and (b) 7 GHz.

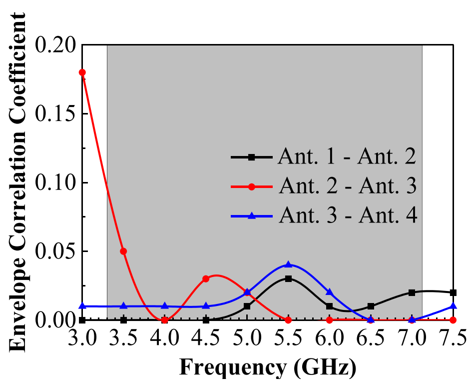

FIGURE 10. Measured ECC of the proposed array antenna (Ant. 1–Ant. 4).

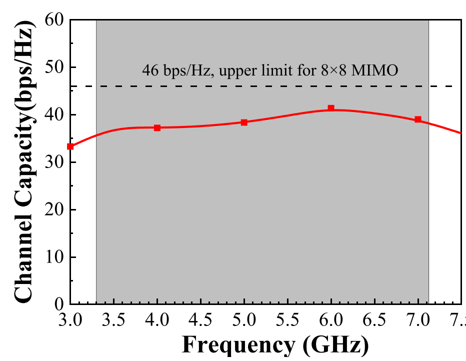

FIGURE 11. The channel capacity of the proposed antenna.

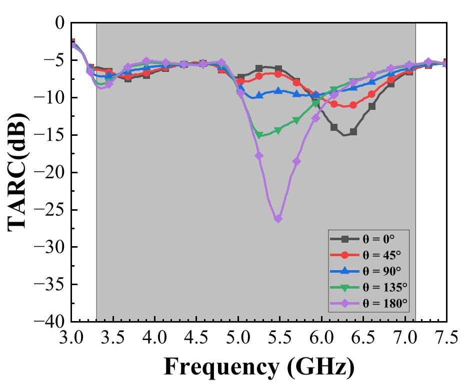

FIGURE 12. The TARC of the proposed antenna.

of 3.3–7.125 GHz, indicating a stable and acceptable radiation capability for practical smartphone applications.

The normalized radiation patterns of Ant. 1 in the X-Z and X-Y planes are shown in Fig. 9 at 3.5 GHz and 7 GHz, respectively. Due to the symmetrical arrangement of the array, only the results for Ant. 1 are presented for brevity. As shown in Figs. 9(a) and (b), the radiation in the X-Z plane is nearly omnidirectional, with a slightly higher gain in the $+X$ direction as the energy radiates outward from the ground plane of the system. Similar characteristics were observed in the X-Y plane. The measured radiation patterns exhibit expected omnidirectional characteristics at 3.5 GHz and 7 GHz. Although pattern variations are observed at higher frequency, the overall directional coverage remains acceptable, verifying the radiation performance of the low-profile design.

5.3. MIMO Performances

The measured Envelope Correlation Coefficients (ECCs) of the proposed array antennas (Ant. 1–Ant. 4) are depicted in Fig. 10. To evaluate the diversity performance and the degree of isolation between the adjacent antenna elements, the ECC is calculated using 3D far-field radiation patterns according to the

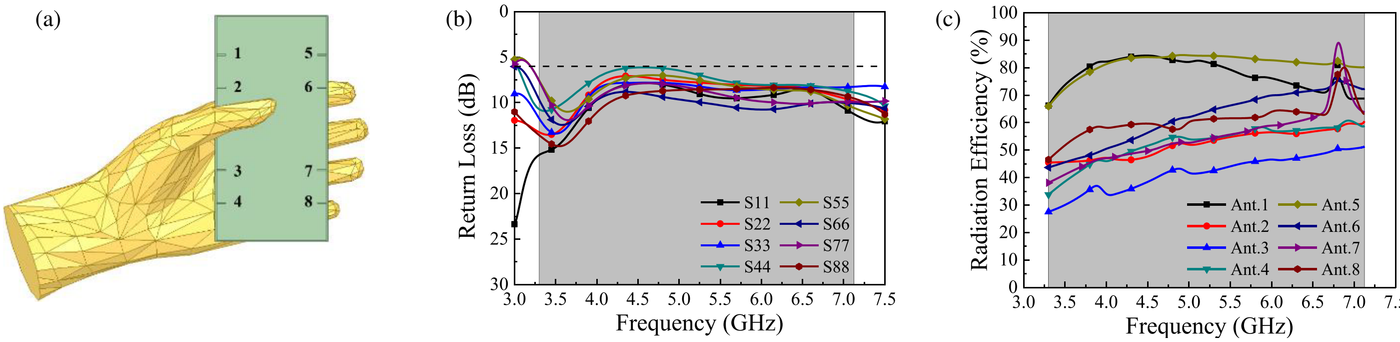

FIGURE 13. Single-handed scenario: (a) simulation setup, (b) simulated return losses, and (c) simulated radiation efficiencies.

following expression [3]:

$$\rho_e = \frac{\left|\iint_{4\pi}\left[\overrightarrow{F_1}(\theta,\varphi) * \overrightarrow{F_2}(\theta,\varphi)\right] d\Omega\right|^2}{\iint_{4\pi}\left|\overrightarrow{F_1}(\theta,\varphi)\right|^2 d\Omega \iint_{4\pi}\left|\overrightarrow{F_2}(\theta,\varphi)\right|^2 d\Omega} \quad (1)$$

As clearly illustrated in Fig. 10, the measured ECC values across the entire operating band are consistently below 0.1. This low value falls well beneath the standard, acceptable threshold of 0.5 for practical MIMO applications. Consequently, the results confirm that the proposed antenna array exhibits low correlation and high pattern diversity between adjacent elements, ensuring robust MIMO system capacity.

The calculated channel capacity of the proposed array antenna in the 8×8 MIMO system is shown in Fig. 11, with values ranging from 35.7 bps/Hz to 41.4 bps/Hz, indicating effective MIMO performance. In this evaluation, the MIMO channel capacity is investigated under an idealized rich-scattering Rayleigh fading environment. The signal-to-noise ratio (SNR) is maintained at a constant 20 dB across the target frequency band. To account for practical correlation and loss effects, a realistic channel matrix **H** is constructed by incorporating the measured ECCs and efficiencies based on the framework described in [27]. Note that the derivation of **H** assumes a 100% element efficiency for the transmitting antenna array. Regarding the receiving array, the symmetric property of the ECC matrix is utilized, and the cross-correlation between distant antenna elements is neglected. Following the determination of the channel matrix, the final MIMO channel capacity C can be evaluated as follows:

$$C = E\left[\log_2 \det\left(\mathbf{I}_N + \frac{\text{SNR}}{N}\mathbf{H}\mathbf{H}^H\right)\right] \quad (2)$$

where **I** denotes the identity matrix; $E[\cdot]$ is the expectation operator; N is the number of receiving and transmitting antennas, respectively; **H** represents the channel gain matrix; and $(\cdot)^H$ denotes the Hermitian transpose. Based on these parameters, the MIMO channel capacity can be directly evaluated under the specified propagation environment.

To evaluate the active impedance matching of the proposed 8-antenna MIMO array under simultaneous excitation, the Total Active Reflection Coefficient (TARC) is investigated. Unlike static S-parameters, TARC accounts for both mutual coupling and input signal phase variations in a realistic environment. According to [26, 28], the TARC between two adjacent ports can be expressed as:

$$\text{TARC}_{12}(\theta) = \sqrt{\left(\frac{\left|S_{11} + S_{12}e^{j\theta}\right|^2 + \left|S_{21} + S_{22}e^{j\theta}\right|^2}{2}\right)} \quad (3)$$

where θ represents the feeding phase difference between the ports. Based on the structural symmetry of the array layout, the representative TARC between Port 1 and Port 2 (TARC_{12}) is calculated using the measured S-parameters. To simulate realistic signal conditions, θ is varied from 0 to 180 degrees with a 45-degree step. The calculated multi-phase TARC_{12} curves are illustrated in Fig. 12. Clearly, all curves remain below the -5 dB threshold across the entire 3.3–7.125 GHz band, with deeper resonance achieved at higher frequencies. These results validate that the proposed antenna array maintains acceptable impedance matching and stable MIMO capability under simultaneous excitation and phase variations in practical applications.

5.4. Effects of Hand and Battery and Performance Comparison Table

Figures 13 and 14 illustrate the impact of the user's hand on the performance of the proposed low-profile array under two standard handheld scenarios: single-handed mode (calling mode) and two-handed mode (reading mode). As shown in Fig. 13(b), the antenna resonant modes exhibited minimal frequency shifts in the single-handed scenario. While antennas in close proximity to the hand, such as Ant. 2, Ant. 3, and Ant. 4, experience a slight variation in return loss, the overall impedance matching remains well within the required operating specifications.

Figure 13(c) presents the simulated antenna efficiency under these loading conditions. Elements positioned further from the hand, such as Ant. 1 and Ant. 5, maintained high efficiency levels. Elements closer to the hand, including Ant. 2, Ant. 6, and Ant. 8, exhibited stable performance. Although Ant. 3 and Ant. 4 experience a reduction in efficiency due to their proximity to the palm tissue, the array as a whole demonstrates sufficient robustness for practical mobile communication. This confirms that the inherent structural configuration of the low-profile antennas effectively balances compact integration with reliable performance in complex user environments.

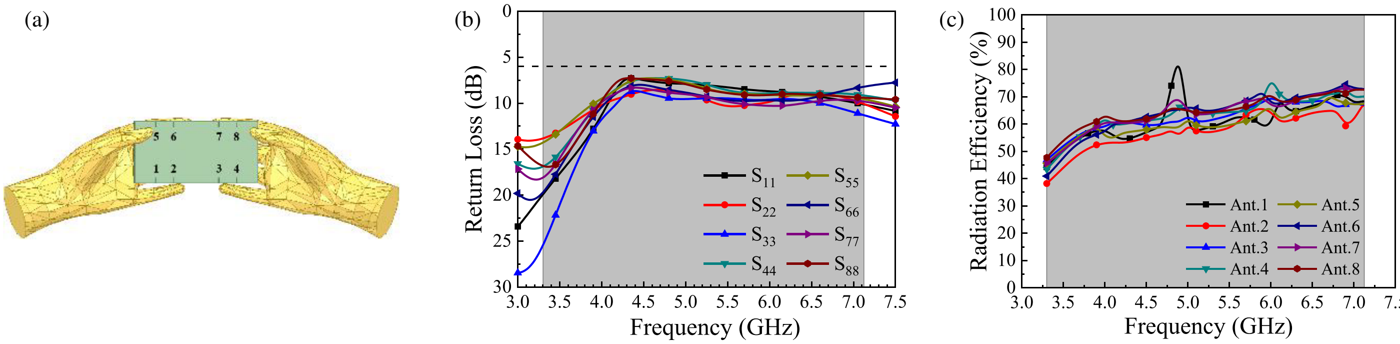

FIGURE 14. Two-handed scenario: (a) simulation setup, (b) simulated return losses, and (c) simulated radiation efficiencies.

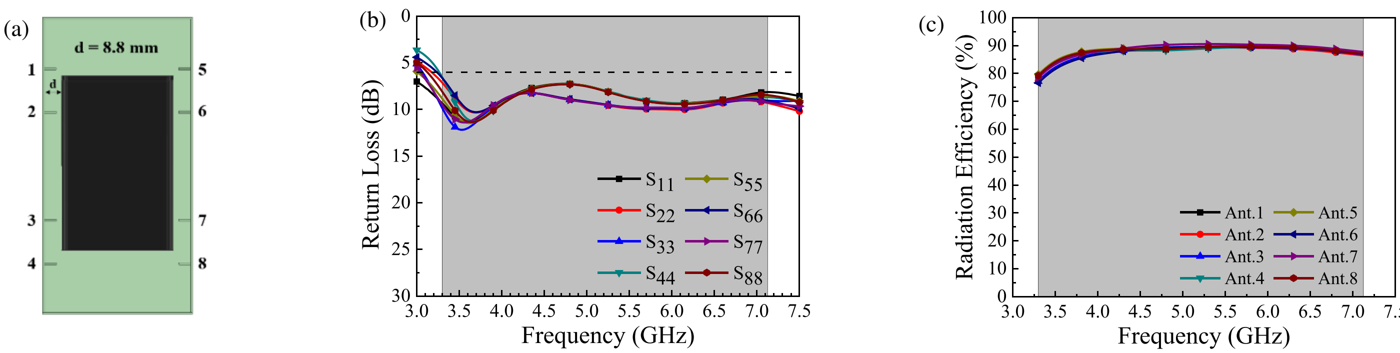

FIGURE 15. Impact of the battery: (a) position of the battery, (b) simulated return losses, and (c) simulated radiation efficiencies.

TABLE 1. Performance comparison table of wideband antenna arrays with metallic frames.

Ref.	Frame Height (mm)	5G Bands (GHz)	Isolation (dB)	Total Efficiency (%)	ECC
[17]	6	5.1–5.9	> 30	4–40	< 0.10
[21]	8.4	3.3–6	> 12.8	50–78	< 0.06
[22]	NA	4.7–4.9	> 14.4	84–90	< 0.02
[23]	7	3.4–3.6, 4.4–5.0, 5.15–5.85	> 16.5	42–82	< 0.18
[24]	7	3.4–5.0	> 16.2	40–82	< 0.11
[25]	6	2.5–3.8, 4.8–7.0, 2.5–6.5	> 12.6	56–90	< 0.18
Proposed	4	3.3–7.125	> 10	40–77	< 0.10

NA: Not Applicable

As shown in Fig. 14(b), the antenna resonant modes exhibited a slight downward frequency shift when held by both hands, which was attributed to the high relative permittivity of human tissue. Despite this effect, the array maintains effective coverage across the 5G NR n77/n78/n79 and 5G NR-U n46/n96 bands. The impact on the antenna efficiency is shown in Fig. 14(c). While Ant. 3 and Ant. 4 experience a more noticeable decrease in efficiency due to their proximity to the palm, the overall efficiency of the array remains acceptable for practical mobile communications. This demonstrates that the low-profile design is sufficiently robust for standard handheld scenarios.

The impact of the internal components was also investigated using a realistic lithium battery model ($76.9 \times 64.2 \times 3.7\,\text{mm}^3$). Fig. 15(a) shows the relative position of the battery within the smartphone frame. As shown in Figs. 15(b) and (c), the presence of the battery does not significantly shift the resonant frequencies or degrade the impedance matching, as it does not obstruct the critical feeding areas of the antenna elements. The antenna efficiency remained stable in the presence of the battery. These results confirm that the inherent structural configuration of the proposed array is highly compatible with the densely packed environments of modern smartphones.

To demonstrate the competitive performance of the proposed antenna array, Table 1 provides a detailed comparison with several state-of-the-art wideband metallic-frame antenna arrays. Compared to the referenced works, the proposed design stands out with the lowest frame height of only 4 mm, representing a significant profile reduction over [17, 21, 23–26]. Despite this low profile, the proposed array achieves the widest continuous frequency coverage (3.3–7.125 GHz), fully supporting the 5G NR and NR-U bands. Furthermore, the proposed antenna exhibits a total efficiency of 40%–77% and maintains an envelope correlation coefficient (ECC) of less than 0.1 across the entire operating band. These results confirm that the proposed array successfully satisfies the practical decoupling and radiation requirements, providing a balanced solution for high-performance MIMO operation in ultra-thin 5G smartphones.

6. CONCLUSION

This study presents the design, fabrication, and characterization of a wideband eight-antenna array for 5G smartphones, specifically optimized for ultra-low-profile metal frames. The proposed antenna element, featuring a unique near-circular slot configuration, achieves continuous wideband coverage across the 5G NR n77/n78/n79 and 5G NR-U n46/n96 bands while maintaining a low height of only 4 mm.

The proposed array employs strategically arranged antenna elements integrated into the metal frame, where the optimized slot configuration promotes pattern diversity and reduces radiation correlation between adjacent elements within the limited available space. Experimental results confirm that the array achieves a low ECC (below 0.1) across the entire target frequency range, demonstrating effective low-correlation MIMO performance. The measured total efficiencies range from 40% to 77% in free space, indicating stable and efficient radiation characteristics across the operating band.

Furthermore, the robustness of the design against hand and battery effects was verified through simulations, confirming reliable performance in practical smartphone environments. The proposed design provides a practical and effective solution for realizing wideband MIMO operation in 4-mm low-profile metal-frame smartphones without requiring complex decoupling structures.

REFERENCES

[1] Parkvall, S., E. Dahlman, A. Furuskar, and M. Frenne, "NR: The new 5G radio access technology," *IEEE Communications Standards Magazine*, Vol. 1, No. 4, 24–30, 2017.

[2] Bleicher, A., "The 5G phone future [News]," *IEEE Spectrum*, Vol. 50, No. 7, 15–16, 2013.

[3] Sharawi, M. S., "Printed multi-band MIMO antenna systems and their performance metrics [wireless corner]," *IEEE Antennas and Propagation Magazine*, Vol. 55, No. 5, 218–232, 2013.

[4] 3GPP, "Technical Specification Group Radio Access Network; NR; User Equipment (UE) radio transmission and reception; Part 1: Range 1 Standalone," 3GPP TS 38.101-1, version 17.12.0 Release 17, 2024.

[5] Shi, H., X. Zhang, J. Li, P. Jia, J. Chen, and A. Zhang, "3.6-GHz eight-antenna MIMO array for mobile terminal applications," *AEU — International Journal of Electronics and Communications*, Vol. 95, 342–348, 2018.

[6] Ban, Y.-L., C. Li, C.-Y.-D. Sim, G. Wu, and K.-L. Wong, "4G/5G multiple antennas for future multi-mode smartphone applications," *IEEE Access*, Vol. 4, 2981–2988, 2016.

[7] Al-Hadi, A. A., J. Ilvonen, R. Valkonen, and V. Viikari, "Eight-element antenna array for diversity and mimo mobile terminal in LTE 3500 MHz band," *Microwave and Optical Technology Letters*, Vol. 56, No. 6, 1323–1327, 2014.

[8] Wong, K.-L., C.-Y. Tsai, and J.-Y. Lu, "Two asymmetrically mirrored gap-coupled loop antennas as a compact building block for eight-antenna MIMO array in the future smartphone," *IEEE Transactions on Antennas and Propagation*, Vol. 65, No. 4, 1765–1778, 2017.

[9] Zhang, X., Y. Li, W. Wang, and W. Shen, "Ultra-wideband 8-port MIMO antenna array for 5G metal-frame smartphones," *IEEE Access*, Vol. 7, 72 273–72 282, 2019.

[10] Cai, Q., Y. Li, X. Zhang, and W. Shen, "Wideband MIMO antenna array covering 3.3–7.1 GHz for 5G metal-rimmed smartphone applications," *IEEE Access*, Vol. 7, 142 070–142 084, 2019.

[11] Chen, H.-D., Y.-C. Tsai, C.-Y.-D. Sim, and C. Kuo, "Broadband eight-antenna array design for sub-6 GHz 5G NR bands metal-frame smartphone applications," *IEEE Antennas and Wireless Propagation Letters*, Vol. 19, No. 7, 1078–1082, 2020.

[12] Li, Y., C.-Y.-D. Sim, Y. Luo, and G. Yang, "Metal-frame-integrated eight-element multiple-input multiple-output antenna array in the long term evolution bands 41/42/43 for fifth generation smartphones," *International Journal of RF and Microwave Computer-Aided Engineering*, Vol. 29, No. 1, e21495, 2019.

[13] Zou, H., Y. Li, B. Xu, Y. Luo, M. Wang, and G. Yang, "A dual-band eight-antenna multi-input multi-output array for 5G metal-framed smartphones," *International Journal of RF and Microwave Computer-Aided Engineering*, Vol. 29, No. 7, e21745, 2019.

[14] Yuan, X.-T., W. He, K.-D. Hong, C.-Z. Han, Z. Chen, and T. Yuan, "Ultra-wideband MIMO antenna system with high element-isolation for 5G smartphone application," *IEEE Access*, Vol. 8, 56 281–56 289, 2020.

[15] Ren, A., Y. Liu, and C.-Y.-D. Sim, "A compact building block with two shared-aperture antennas for eight-antenna MIMO array in metal-rimmed smartphone," *IEEE Transactions on Antennas and Propagation*, Vol. 67, No. 10, 6430–6438, 2019.

[16] Sun, L., Y. Li, Z. Zhang, and Z. Feng, "Wideband 5G MIMO antenna with integrated orthogonal-mode dual-antenna pairs for metal-rimmed smartphones," *IEEE Transactions on Antennas and Propagation*, Vol. 68, No. 4, 2494–2503, 2020.

[17] Abdelgwad, A. H. and M. Ali, "Smartphone metal-casing integrated frequency-reconfigurable multiple-input multiple-output slot antenna," *International Journal of RF and Microwave Computer-Aided Engineering*, Vol. 32, No. 11, e23389, 2022.

[18] Yuan, X.-T., Z. Chen, T. Gu, and T. Yuan, "A wideband PIFA-pair-based MIMO antenna for 5G smartphones," *IEEE Antennas and Wireless Propagation Letters*, Vol. 20, No. 3, 371–375, 2021.

[19] Zhao, A. and Z. Ren, "Size reduction of self-isolated MIMO antenna system for 5G mobile phone applications," *IEEE Antennas and Wireless Propagation Letters*, Vol. 18, No. 1, 152–156, 2019.

[20] Fang, Y., Y. Liu, Y. Jia, and J. Liang, "Deca-band structure reutilization MIMO antenna for 4G/5G full-screen metal frame smartphone operation," *International Journal of RF and Microwave Computer-Aided Engineering*, Vol. 31, No. 12, e22890, 2021.

[21] Fakharian, M. M., "A low-profile compact UWB antenna array for sub-6 GHz MIMO applications in 5G metal-frame smart-

phones," *International Journal of RF and Microwave Computer-Aided Engineering*, Vol. 32, No. 10, e23320, 2022.

[22] Sufyan, A., S. A. A. Shah, K. B. Khan, I. A. Shah, A. Ullah, T. A. Siddiqui, S. Islam, and H. Yoo, "Self-decoupled 8-element dual polarized MIMO antenna for B5G handsets with sub-6 GHz and mmWave integration," *IEEE Access*, Vol. 12, 167 324–167 332, 2024.

[23] Li, H., S. Xiao, L. He, Q. Cai, and G. Liu, "A dual-band 8-antenna array design for 5G/WiFi 5 metal-frame smartphone applications," *Micromachines*, Vol. 15, No. 5, 584, 2024.

[24] Kong, Q., P. Zhang, L. Chen, and J. Bai, "High-isolation compact wideband MIMO antennas for 5G smartphones with unbroken metal frames," *Electronics*, Vol. 14, No. 19, 3852, 2025.

[25] Chen, L., J. Bai, and H. Gu, "Design of an ultra-wideband MIMO antenna with open-slot structures for 5G metal-frame smartphones," *Sensors*, Vol. 25, No. 19, 5973, 2025.

[26] Addepalli, T., V. S. Nagaraju, S. Medasani, J. C. Rao, P. Badugu, C. M. Kumar, R. Uppada, and B. K. Kumar, "Four-element equilateral triangular-shaped MIMO antenna with connected ground for 5G sub: 6 GHz N79 and WiFi-6E band applications," *International Journal of Communication Systems*, Vol. 37, No. 16, e5895, 2024.

[27] Hu, W., X. Liu, S. Gao, L.-H. Wen, L. Qian, T. Feng, R. Xu, P. Fei, and Y. Liu, "Dual-band ten-element MIMO array based on dual-mode IFAs for 5G terminal applications," *IEEE Access*, Vol. 7, 178 476–178 485, 2019.

[28] Addepalli, T., T. Vidyavathi, K. Neelima, M. Sharma, and D. Kumar, "Asymmetrical fed Calendula flower-shaped four-port 5G-NR band (n77, n78, and n79) MIMO antenna with high diversity performance," *International Journal of Microwave and Wireless Technologies*, Vol. 15, No. 4, 683–697, 2023.